Supplementary Information

Full electric-field tuning of the nonreciprocal transport effect in massive chiral fermions with trigonal warping

Elisha Cho-Hao Lu, Liang Li, Cheng-Tung Cheng, and Wei-Li Lee

In this supplementary information, there are five sections listed below.

1. The sheet density and Hall mobility from Hall measurements.
2. Discussions of the possible PN semiconducting junction effect.
3. Calculations of the second harmonic conductance $\sigma_{2\omega}$ based on the Boltzmann transport equation.
4. The measurements of $R_{2\omega}$ in other dual-gated BLG devices.
5. The frequency-dependent of the R_ω and $R_{2\omega}$ and a comparison to results from pulsed DC measurements.

1. The sheet density and Hall mobility from Hall measurements.

To characterize the properties of the bilayer graphene sample, we have performed Hall measurements at $T = 5$ K with $V_{tg} = 0$. The Hall resistance was found to be field-linear in weak fields up to 0.5 Tesla, and the corresponding sheet density n_{2D} was obtained from the Hall coefficient $R_H = \frac{1}{n_{2D}e}$, where e is the elementary charge. We measured the Hall resistance at 0.5 T and -0.5 T and estimated the carrier density with respect to V_{bg}, as shown in the supplementary Fig. S1(a). We have also tried to evaluate the capacitance of bottom-gate in our dual-gated device. The capacitance $C = \frac{\Delta n_{2D}e}{\Delta V_{bg}}$ can be determined from the slope for the curve of carrier density as a function of voltage of bottom-gate. The capacitance values in the electron-doping and hole-doping regions are around 91.34 aF/μm^2 and 109.72 aF/μm^2, respectively, which are well consistent with the nominal value of around 110 aF/μm^2 estimated from simple parallel plate capacitor model. The corresponding mobility μ as a function of bottom-gate is shown in the supplementary Fig. S1(b), using the relation of conductivity $\sigma = n_{2D}e\mu$. The mobility is more than 10,000 cm^2/Vs in the electron-doping region, and it is slightly higher for the hole doping region. we do note some anomaly in the hole doping region near $n_{2\mathrm{D}} = 0.5$ - $1.0 \times 10^{12} cm^{-2}$, which is likely due to the contribution from top-gate ineffective regions between the voltage leads.

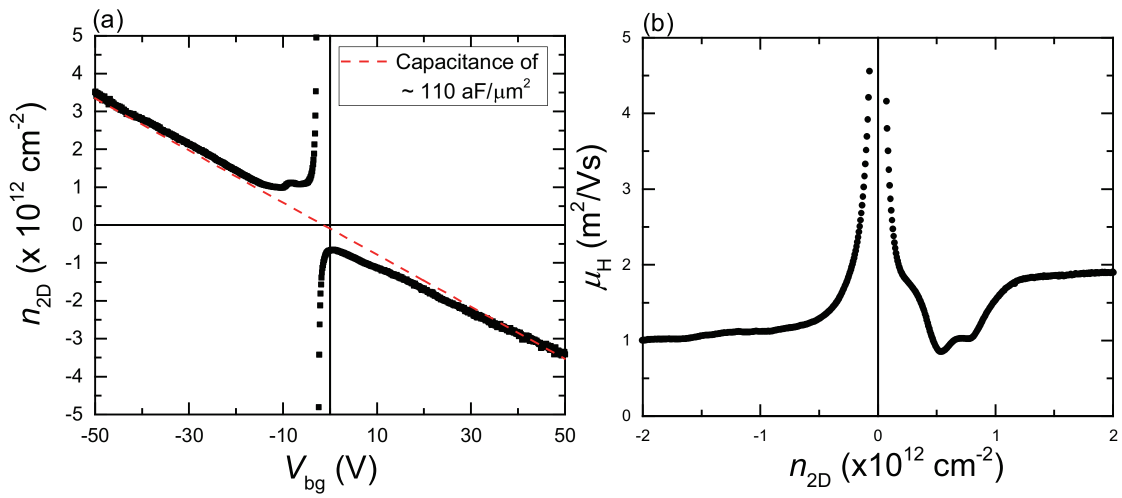

FIG. S1: Hall effect measurements. (a) The sheet density n_{2D} as a function of V_{bg}. The red dashed-line is a curve with a capacitance of $\approx$ 110 aFμm^{-2} via the bottom-gate. (b) The extracted mobility μ as a function of V_{bg}.

2. Discussions of the possible PN semiconducting junction effect.

Electron/hole doping concentration in BLG is manipulated by a top-gate and a bottom-gate. The silicon wafer is used as a bottom-gate, so the whole area of BLG is affected by the bottom-gate. However, the area of the top-gate is limited and only a part of BLG can be affected by the top-gate, as shown in the Fig. 1(a) of the main text. Thus, the BLG device is divided into three regions as illustrated in the supplementary Fig. S2(a), where only the middle region is top-gate effective and the other two regions are only bottom-gate effective (or top-gate ineffective). The sheet resistance (R_ω) as a function of $V_{\rm bg}$ and $V_{\rm tg}$ at 5 K is shown in the supplementary Fig. S2(b). The dashed line shows the locations for R_ω peaks and corresponds to the charge neutrality for the top-gate effective region of a gapped BLG. The solid line represents $V_{\rm bg} = V_{\rm bg0}(\approx -1.86V)$ that gives a maximum R_ω at zero $V_{\rm tg}$, which separates the P-type and N-type phases for the top-gate ineffective regions. These two lines divide the resistance map into four phases, representing four different combinations of NNN, NPN, PPP, and PNP based on the Fermi level location as illustrated in the supplementary Fig. S2(a). It is known that a PN junction results in current rectification effect. However, our dual-gated device comprises two PN junctions that work more like a transition with

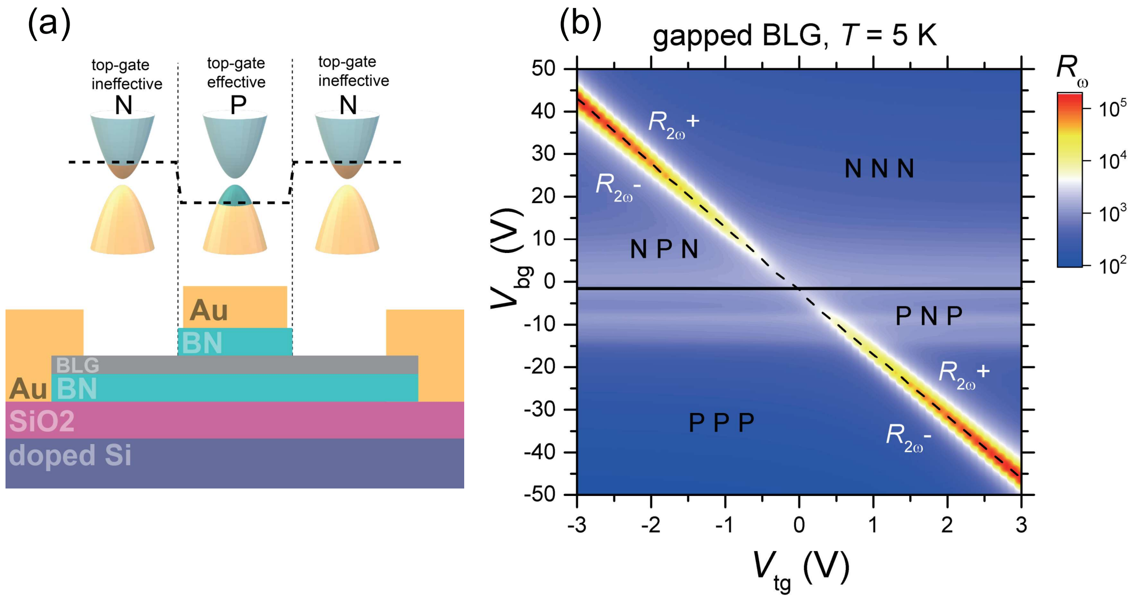

FIG. S2: Semiconducting PN phase diagram of a dual-gated BLG device. (a) An illustration of a dual-gated BLG device with top-gate effective and ineffective regions. (b) Sheet resistance of BLG as a function of bottom-gate and top-gate at 5K. The dashed black line is a visual guide showing the charge neutrality of top-gate effective region. The dashed and solid black lines divide the phase diagram into four parts of different polarities. The observed sign of the $R_{2\omega}$ is also marked in (b).

gate-tunable conductance across the device, and it is not likely to exhibit current-directional-dependent resistance for a single PN-junction. Starting from NPN phase for example, the conductance reaches a minimum near the dashed-line region when moving along the D-constant line to NNN phase as expected for a transistor-like behavior. Supposedly, there is somehow a difference in the two top-gate ineffective regions (supplementary Fig. S2(a)), and it thus may cause certain current-directional-dependent effects. It still cannot explain the observed complex $R_{2\omega}$ behaviors as described in the main text, including the sign changes and also the rapid decays of its magnitude away from the band edges. Combining with the fact that R_ω is nearly I independent as shown in Fig. 2(a) of the main text, we, therefore, argue that the observed large $R_{2\omega}$ is not likely due to the trivial PN semiconducting junction or diode-related effects.

3. Calculations of the second harmonic conductance $\sigma_{2\omega}$ based on the Boltzmann transport equation.

The equilibrium Fermi-Dirac distribution function is given by $f_0 = \frac{1}{e^{(\epsilon-\mu)/k_B T}+1}$. The total electron distribution is $f_{\vec{\mathrm{k}}} = f_0 + g_{\vec{\mathrm{k}}}$, where $g_{\vec{\mathrm{k}}}$ refers to the non-equilibrium distribution function. Using a relaxation approximation with $\left(\frac{\partial f_{\vec{\mathrm{k}}}}{\partial t}\right)_{\mathrm{collision}} = -\frac{g_{\vec{\mathrm{k}}}}{\tau}$, we set $\vec{E} = E_{\mathrm{x}}\hat{\imath}$ and keep terms up to E^2 for $g_{\vec{\mathrm{k}}}$, and then

$$\begin{aligned} g_{\vec{\mathrm{k}}} &= -\frac{q\vec{E}\tau}{\hbar} \cdot \frac{\partial(f_0+g_{\vec{\mathrm{k}}})}{\vec{k}} \\ &\approx -\frac{qE_{\mathrm{x}}\tau}{\hbar}\frac{\partial f_0}{\partial k_{\mathrm{x}}} + \left(\frac{qE_{\mathrm{x}}\tau}{\hbar}\right)^2 \frac{\partial^2 f_0}{\partial k_{\mathrm{x}}^2}. \end{aligned} \tag{S1}$$

The current density for a two dimensional system is then

$$\begin{aligned} j_{\mathrm{x}} &= 2q\int v_{\vec{\mathrm{k}}} g_{\vec{\mathrm{k}}} \frac{d^2\vec{k}}{(2\pi)^2} \\ &= \left[-\frac{q^2}{\hbar}\int \frac{d^2\vec{k}}{2\pi^2}\tau v_{\vec{\mathrm{k}}}\frac{\partial f_0}{\partial k_{\mathrm{x}}}\right] E_{\mathrm{x}} + \left[\frac{q^3}{\hbar^2}\int \frac{d^2\vec{k}}{2\pi^2}\tau^2 v_{\vec{\mathrm{k}}}\frac{\partial^2 f_0}{\partial k_{\mathrm{x}}^2}\right] E_{\mathrm{x}}^2 \\ &\equiv \sigma_\omega E_{\mathrm{x}} + \sigma_{2\omega} E_{\mathrm{x}}^2. \end{aligned} \tag{S2}$$

Therefore, the second harmonic conductance can be expressed as [1]

$$\begin{aligned} \sigma_{2\omega} &= \frac{q^3}{\hbar^2}\int \frac{d^2\vec{k}}{2\pi^2}\tau^2 v_{\vec{\mathrm{k}}}\frac{\partial^2 f_0}{\partial k_{\mathrm{x}}^2} \\ &= \frac{q^3\tau^2}{2\pi\hbar}\oint dS_{\mathrm{F}} \cos^3\varphi \left[3\frac{|v_{\mathrm{k}}|}{v_{\mathrm{k}}}\frac{\partial v_{\mathrm{k}}}{\partial p} - \frac{\partial |v_{\mathrm{k}}|}{\partial p}\right]_{\varepsilon_{\mathrm{F}}} \\ &\equiv \frac{q^3\tau^2}{2\pi\hbar^2} I_{2\omega}, \end{aligned} \tag{S3}$$

where $dS_{\mathrm{F}} = p\, d\phi/\hbar$ at Fermi surface, $v_{\mathrm{k}} = \partial\varepsilon/\partial p$ and $I_{2\omega} \equiv \oint d\phi\; p\cos^3\phi\; [3\frac{|v_{\mathrm{k}}|}{v_{\mathrm{k}}}\frac{\partial v_{\mathrm{k}}}{\partial p} - \frac{\partial|v_{\mathrm{k}}|}{\partial p}]_{\varepsilon_{\mathrm{F}}}$ is the path integral along closed Fermi surfaces. Here, we assume that τ is independent of p and ϕ.

By numerically calculating v_{k} and $\partial v_{\mathrm{k}}/\partial p$ for a gapped BLG with trigonal warping, $I_{2\omega}$ and thus $\sigma_{2\omega}$ can be obtained. Using the energy dispersion for a gapped BLG with trigonal warping (Eq. 1 in the main text), the $I_{2\omega}$ term can be numerically calculated and shown in the upper-panels of supplementary Fig. S3(a) and (b) for two different asymmetry parameters of $\Delta = 10$ meV and 30 meV, respectively, where the corresponding calculated sheet densities $n_{2\mathrm{D}}$ are shown in the lower-panel. The inset cartoons show the corresponding Fermi surfaces in different ε_{F} regimes. For $\Delta = 10$ meV (supplementary Fig. S3(a)), there are two Lifshitz transitions at energies of $\varepsilon_{\mathrm{L1}}$ and $\varepsilon_{\mathrm{L2}}$. $\varepsilon_{\mathrm{L1}}$ equals ≈ 5.09 meV, corresponding to a transition from a single Fermi surface (black-line) to four separated Fermi surfaces (Blue-line). As ε_{F} keeps decreasing, another transition into three separated Fermi surfaces

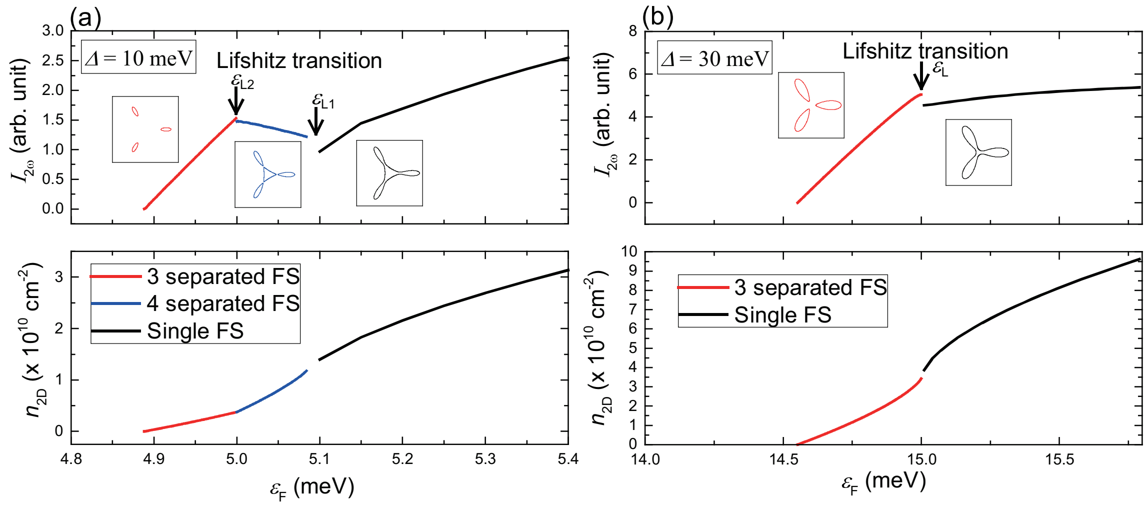

FIG. S3: The numerically calculated $I_{2\omega}$and $n_{2\mathrm{D}}$ for $K+$ valley at different values of asymmetry parameter Δ. The calculated $I_{2\omega}$and $n_{2\mathrm{D}}$ as a function of the Fermi energy ε_{F} is plotted in the upper-panel and lower-panel of (a) for Δ = 10 meV, respectively. (c) shows the calculated $I_{2\omega}$and $n_{2\mathrm{D}}$ for Δ = 30 meV.

(red-line) occurs at $\varepsilon_{\mathrm{L2}} \approx 5.00$ meV. The supplementary Fig. S3(b) shows the results for Δ = 30 meV, where only one Lifshitz transition from a single Fermi surface to three separated Fermi surfaces was observed at $\varepsilon_{\mathrm{L}} \approx 15$ meV. We note that both calculated $I_{2\omega}$ and $n_{2\mathrm{D}}$ values show abrupt changes at Lifshitz transition energies. The sheet density at $\varepsilon_{\mathrm{L1}}$ (ε_{L}) for Δ = 10 meV (30 meV) equals ≈ 1.3 (3.9) $\times$ 10^{10} cm^{-2}, which turns out to increase gradually with Δ. Within our experimental D values, the sheet density at Lifshitz transition is expected to be in the range of $\approx 1 - 10 \times 10^{10}$ cm^{-2}, which is in the same order of magnitude as the sheet density that we observed in experiment for the occurrence of a maximum $|R_{2\omega}|$ (Fig. 3(d) in the main text).

The measured quantity of $R_{2\omega}$ can be related to σ_ω and $\sigma_{2\omega}$ by inverting the current density equation shown in Eq. S2 [2], giving

$$E_{\mathrm{x}} \approx [1/\sigma_\omega] j_{\mathrm{x}} - [\sigma_{2\omega}/\sigma_\omega^3] j_{\mathrm{x}}^2. \tag{S4}$$

Therefore, the magnitude of measured second harmonic sheet resistance $R_{2\omega}$ can be shown to be

$$R_{2\omega} \equiv \frac{V_{2\omega}}{I_0}\frac{W}{L} = -\frac{I_0}{W}\frac{\sigma_{2\omega}}{\sigma_\omega^3}, \tag{S5}$$

where $V_{2\omega}$ is the measured second harmonic voltage, I_0 is the magnitude of the driving current, and $W(L)$ is the device width (length between voltage electrodes).

4. The measurements of $R_{2\omega}$ in other dual-gated BLG devices.

Several dual-gated BLG devices were fabricated and showed consistent results as described in the main text. In the supplementary Fig. S4(a), we put the measured $R_{2\omega}$ signals for one dual-gated BLG device with a lower Hall mobility of $\approx$ 8,000 cm^2/Vs, where the top and bottom hBN layer thicknesses are 28.4 nm and 11 nm, respectively. The $R_{2\omega}$ shows again a peak near the conduction band edge and then rapidly drops to a valley near the valence band edge when moving along the D-constant contour-line, which is in accord with the behaviors described in the main text. The mosaic-like pattern in the supplementary Fig. S4(a) is due to insufficient data points in between. The corresponding scaling plot of $R_{2\omega}$ versus R_ω in a logarithmic scale is shown in the supplementary Fig. S4(b). It gives a relation of $R_{2\omega} \propto R_\omega^{1.32}$, where the exponent ($\lambda = 1.32$) appears to be smaller than the device described in the main text. The device-dependent λ suggests that the charge-puddle effect plays a role on affecting the observed magnitude of R_ω. The impurity charges and potential fluctuations due to charge puddles in a gapped BLG may enhance the conductance and thus reduce R_ω values near the band edges, which can be more significant in low D regime. We suspect that this effect may somehow enlarge the spanning for R_ω when tuning D, giving rise to a reduced λ value.

5. The frequency-dependent of the R_ω and $R_{2\omega}$ and a comparison to results from pulsed DC measurements.

For AC measurements, a change in the driving frequency turns out to cause a variation in both measured R_ω and $R_{2\omega}$. The frequency dependents of R_ω and $R_{2\omega}$ are shown in the supplementary Fig. S5(a) and (b), respectively. Both R_ω and $R_{2\omega}$ drops with increasing driving frequency, where the decay in $R_{2\omega}$ with increasing frequency appears to be more significant. This indicates the capacitance effect in our measurements circuits, which is

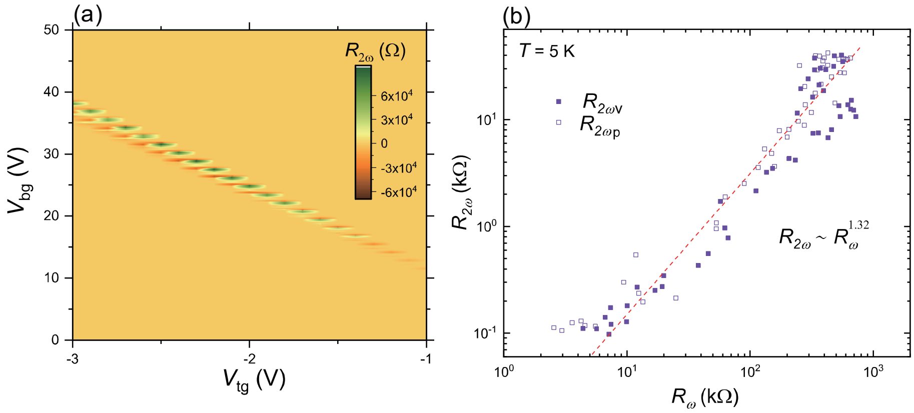

FIG. S4: The measured $R_{2\omega}$ for another dual-gated BLG device. (a) The $R_{2\omega}$ as a function of V_{bg} and V_{tg} at $T = 5$ K, which shows a consistent behavior as described in the main text. The scaling plot of $R_{2\omega}$ versus R_{ω} gives an exponent $\lambda \approx 1.32$.

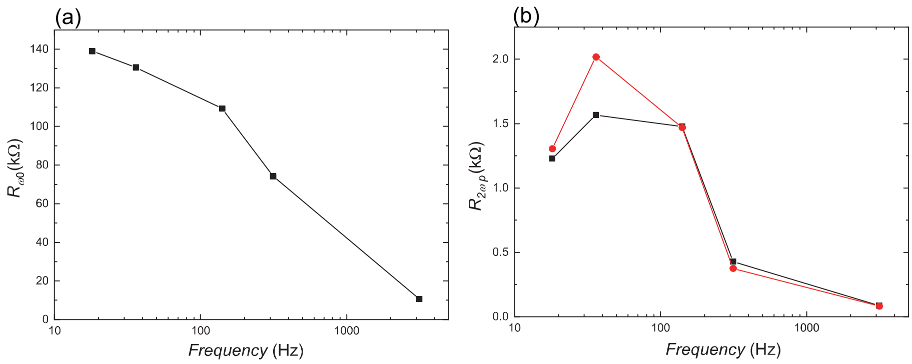

FIG. S5: Frequency dependent of the measured signals. (a) and (b) are the first harmonic sheet resistance and the second harmonic resistance, respectively, as a function of AC driving frequency in logarithmic -scale.

likely deriving from the contact and gate electrodes. Therefore, the AC measurements for probing the NRTE in dual-gated devices should be carried out in low frequency regime to avoid the shunting of the current via the capacitive coupling to electrodes. We note that this is particularly important for the measurements near the band edges in high D regime, where the sheet resistance of a gapped BLG rises up rapidly.

Probing NRTE by pulsed DC measurements: We have also performed pulsed DC measurement to confirm the nonreciprocal transport effect. One of the concern of DC pulse measurement is the onset of excitation. When the current excitation is suddenly lifted from zero to a set point, there is a finite rise time for the responding voltage. In order to minimize the Joule heating effect, proper width for the current pulse and also suitable delay time are carefully chosen to ensure a reliable measurement. For consistency, at each $V_{\rm bg}$ setpoint, the resistance data derives from statistical average data of 50 pulsed DC measurements, where each measurement comprises a current pulse of 10 ms width and a voltage measurement with 8 ms source delay. The measured resistance as a function of bottom-gate through DC pulse mode measurement using 20 nA and -20 nA under $V_{tg} = -2.5$ V are shown in the supplementary Fig. S6(a), which demonstrates an observable difference in the resistance near the local maximum of R_ω. Thus, the current-direction-dependent resistance is again verified under pulsed DC measurement. The resistance change $\Delta R = R_{\rm 20nA} - R_{\rm -20nA}$ as a function of bottom-gate with $V_{tg} = -2.5$ V and 2.5 V are plotted in the supplementary Fig. S6(b) and (c), respectively. A noticeable ΔR happens near $V_{bg} = 35$ V with $V_{tg} = -2.5$ V and $V_{bg} = -39$ V with $V_{tg} = 2.5$ V. ΔR changes sign when the type of carrier changes. The observed ΔR first attains a peak and then drops rapidly to reach a valley as gate voltage decreases. Those results are consistent with the behavior in AC measurements shown in the main text.

[1] Ziman, J.M. *Principle of the Theory of Solids* Ch.2 (Cambridge Univ. Press,1972).

[2] Yasuda K. *et al.* Large unidirectional magnetoresistance in a magnetic topological insulator. *Phys. Rev. Lett.* **117,** 127202 (2016).

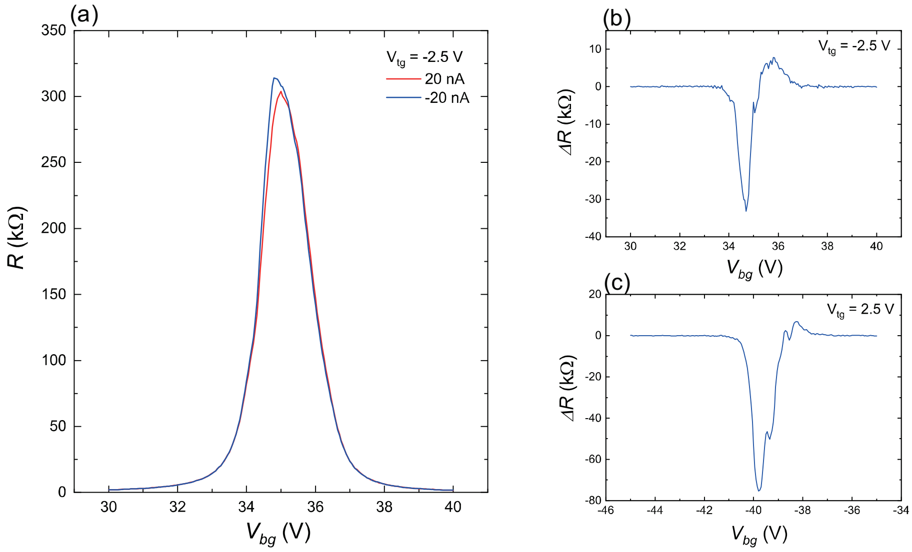

FIG. S6: Pulsed DC measurements. (a) Sheet resistance as a function of bottom-gate with the top-gate fixed at -2.5 V using opposite current directions by DC pulse measurement. (b) and (c) show the difference of sheet resistances as a function of bottom-gate with top-gate values fixed at -2.5 V and 2.5 V, respectively.